Nanoscale

PAPER

View Article Online
View Journal | View Issue

Cite this: *Nanoscale*, 2025, **17**, 2700

Atomic spin precession electro-optic modulation detection based on guided mode resonant lithium niobate metasurfaces†

Jie Sun,[a,b,c,d] Zhen Chai,[a,b,c,d]* Yuqing Yang,[e] Zhibo Cui,[a,b,c,d] Yuting Xu,[a,b,c,d] Yan Xu,[a,b,c,d] Yulan Fu[e] and Heng Yuan*[f]

Received 15th November 2024,
Accepted 30th December 2024

DOI: 10.1039/d4nr04794j

rsc.li/nanoscale

Low-frequency noise in detection systems significantly affects the performance of ultrasensitive and ultra-compact spin-exchange relaxation-free atomic magnetometers. High frequency modulation detection helps effectively suppress the 1/*f* noise and enhance the signal-to-noise ratio, but conventional modulators are bulky and restrict the development of integrated atomic magnetometer modulation-detection systems. Resonant metasurface-based thin-film lithium-niobate (TFLN) active optics can modulate free-space light within a compact configuration. In this study, we demonstrate a TFLN metasurface platform that leverages guided mode resonance for efficient phase modulation, achieving a modulation amplitude of 0.063 rad at a frequency of 100 kHz. We exploit the resonance in the TFLN waveguide and obtain a high-quality factor of 166 at a resonant wavelength of 795.8 nm. Using the fabricated modulator, we achieve an optical rotation angle measurement sensitivity of 4×10^{-7} rad $Hz^{-1/2}$ with the modulation. Compared to conventional bulky modulators, the modulator fabricated in this study realizes more than 90% reduction in volume. This study provides a feasible approach for developing miniaturized integrated atomic magnetometers to achieve ultrahigh sensitivity through optical modulation techniques.

1. Introduction

Atomic magnetometers based on the spin-exchange relaxation-free (SERF) state have significant applications in biomagnetism sensing,[1–3] inertial measurement,[4] and fundamental physical experiments,[5] owing to their ultrahigh theoretical sensitivity and lack of cryogenic cooling requirements. In recent years, research has focused on developing chip-scale optically pumped magnetometers that use microfabricated rather than conventional optical components, with the aim of achieving higher spatial resolution in magnetocardiography and magnetoencephalography measurements.[6–10] Although replacing bulky optical components with compact metasurfaces facilitates integration, most of these components are static and do not contribute to improving the detection sensitivity of miniaturized atomic sensors. Conventional methods, such as balanced polarimetry, offer the simplest optical configurations but fail to isolate low-frequency noise within the detection system, making the output signal highly susceptible to 1/*f* noise.[7–11,16] Consequently, the sensitivity and long-term stability of the atomic sensors are significantly limited. Table 1 presents a comparison of sensitivity with and without modulation. Compared with without modulation, optical modulation detection methods offer significant advantages in suppressing low-frequency noise, enhancing sensitivity, and mitigating magnetic field crosstalk.[12–15] However, the integration of optical systems is constrained by the large sizes of conventional modulators. Notably, the required modulation amplitude $\alpha_m \ll 1$ rad for optical modulation detection methods used in atomic magnetometers.[13,28] Recently, metasurfaces composed of subwavelength structures combined with auxiliary optimization algorithms[17] have attracted great attention for achieving precise control of the phase, polarization, and amplitude of electromagnetic waves,[8–10] as well as for enabling all-optical signal processing.[18,19] Advancements in the utilization of the electro-optic Pockels effect combined with metasurface resonant structures to modulate the refractive indices

[a]*Key Laboratory of Ultra-Weak Magnetic Field Measurement Technology Ministry of Education, School of Instrumentation and Optoelectronic Engineering, Beihang University, Beijing, 100191, China. E-mail: zhenchai@buaa.edu.cn*
[b]*Institute of Large-scale Scientific Facility and Centre for Zero Magnetic Field Science, Beihang University, Beijing, 100191, China*
[c]*Hangzhou Extremely Weak Magnetic Field Major Science and Technology Infrastructure Research Institute, Hangzhou, 370051, China*
[d]*Beihang Hangzhou Innovation Institute, Hangzhou, 370052, China*
[e]*Institute of Information Photonics Technology, School of Physics and Optoelectronic Engineering, Beijing University of Technology, Beijing, 100124, P.R. China*
[f]*School of Instrumentation and Optoelectronic Engineering, Beihang University, Beijing 100191, China. E-mail: hengyuan@buaa.edu.cn*

†Electronic supplementary information (ESI) available: The image of the sample, additional simulation and experimental results, and photographs of the experimental setup. See DOI: https://doi.org/10.1039/d4nr04794j

Table 1 Comparison of sensitivity with and without modulation

Ref.	Detection method	Sensitivity	Atomic source	Frequency
15	Electro-optic modulation	2.3 fT $Hz^{-1/2}$	^{87}Rb–^{4}He	10 Hz
	Balanced polarimetry	7.1 fT $Hz^{-1/2}$		
40	Electro-optic modulation	10 fT $Hz^{-1/2}$	K–Rb–^{4}He	30 Hz
	Balanced polarimetry	30 fT $Hz^{-1/2}$		
46	Acousto-optic modulation	14.3 fT $Hz^{-1/2}$	K–Rb–^{4}He	30 Hz
	Balanced polarimetry	26.79 fT $Hz^{-1/2}$		

of specific ferroelectric materials have enabled rapid electrical control[20] and effective phase modulation.[29] Spatial light modulators based on electro-optic materials have demonstrated superior modulation performances in compact configurations. Thin-film lithium niobate (TFLN) exhibits strong optical confinement and enhanced customizability, enabling performance levels that are unattainable with bulk lithium niobate (LN), such as CMOS-compatible driving voltages and high-bandwidth operations.[21] These attributes highlight the advantages of miniaturization and integration. Owing to the broad transparency window of LN, electro-optic TFLN devices have shown effectiveness in the near-infrared region.[22,23] However, limitations in the available interaction region lead to low tunability and modulation depth,[20] and the integration of sub-wavelength resonators is crucial for achieving efficient modulation. Techniques such as realizing quasi-bound states in the continuum,[24] plasmonic resonances,[25] and Mie resonances[26,27] at the nanoscale are essential for enhancing these interactions. Moreover, recent studies have revealed that, in addition to the aforementioned resonant structures, all-dielectric metasurfaces based on guided mode resonance (GMR) provide an effective means of achieving a high-quality (Q) factor.[31]

In this work, we show the potential of a microfabricated electro-optic modulator (EOM) to modulate low-frequency atomic spin precession signals at high frequency. A compact EOM based on GMR was designed and fabricated, enabling the realization of an electro-optic modulation detection system capable of high-frequency modulation of extremely small optical rotation angle signals. The GMR is achieved through the interaction of optimized nanopillar dimensions with TFLN, resulting in strong field localization within the resonant structure. A resonance depth of approximately 60% was achieved near the 795 nm working wavelength. Experimental results demonstrated a phase modulation amplitude of approximately 0.063 rad at a modulation frequency of 100 kHz under a sinusoidal alternating current (AC) drive voltage. With high frequency modulation using the fabricated modulator, the sensitivity of the optical rotation angle measurement increased from 5×10^{-6} rad $Hz^{-1/2}$ to 4×10^{-7} rad $Hz^{-1/2}$ compared to without modulation. A conceptual sketch of the atomic spin precession detection using the proposed integrated EOM modulator is depicted in Fig. 1(a). As presented in this sketch, the EOM can be integrated with other nanoscale devices such as polarizers and waveplates.[32] Thus, the modulator is no longer a bulky external device and can be integrated into a chip-scale magnetometer.

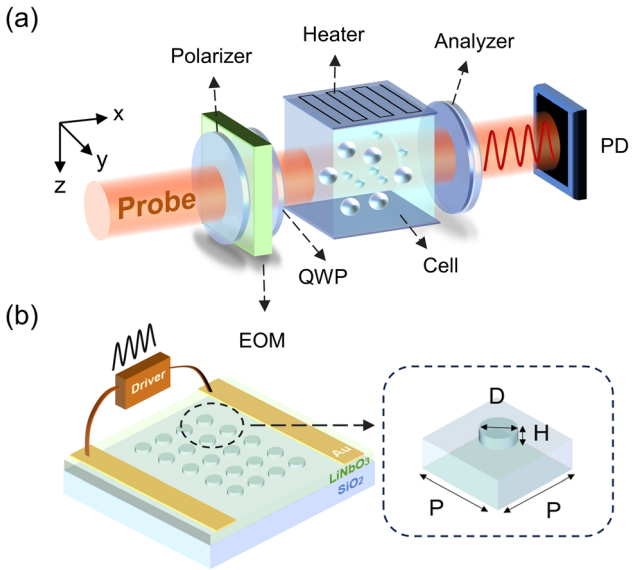

Fig. 1 EOM concept and design. (a) Conceptual sketch of the electro-optic modulation detection system based on a compact device. QWP: quarter-wave plate; PD: photodetector. (b) Schematic of the integrated EOM based metasurface. The amplified area is the basic unit of the nanopillar.

2. Design and methods

A compact SERF magnetometer typically uses Rb atoms as sensitive sources that respond to magnetic fields. The electron spins of the alkali metal atoms are polarized along the direction of propagation (z-axis) of the pump light (frequency tuned to the D1 line of the Rb atoms at 794.979 nm). Atomic spin precession occurs when an external magnetic field is applied. The spin component S_x can be obtained using a linearly polarized probe beam by detuning, which propagates in the x-direction.[33] The optical rotation angle reflecting S_x of the alkali metal Rb atom is expressed as follows:[34,35]

$$\theta = l r_e n c f_{D1} S_x \frac{\nu_p - \nu_0}{(\nu_p - \nu_0)^2 + (\Gamma_{D1}/2)^2} \quad (1)$$

where l is the length of the probe beam passing through the alkali–metal cell, r_e is the classical electron radius, n is the density of the Rb atoms, c is the speed of light, and f_{D1} denotes the oscillator strength of the D1 transition of alkali metal atoms. The frequency of the probe laser is denoted by

ν_p, the resonant frequency of the Rb D1 line is denoted by ν_0, and the pressure broadened linewidth is expressed as Γ_{D1}.

The optical rotation θ can be detected by the EOM detection system as shown in Fig. 1(a). The probe laser propagates along the x-axis and first passes through a polarizer, whose transmission axis is parallel to the y-axis. The laser is modulated by the fabricated compact EOM driven by a high frequency input signal, and a quarter-wave plate with its axis parallel to the polarizer in the beam path. An optical rotation angle θ emerges after the modulated laser passes through the cell. Subsequently, the light intensity is converted by an analyzer whose transmission axis is perpendicular to the polarizer, and the transmitted light is converted into an electrical signal by a photodetector. The output signal is demodulated using a digital lock-in amplifier at the modulation frequency to achieve precise measurements.

To derive the relationship between the optical rotation angle θ and the system output, a simple theoretical model of the EOM detection system is established using the Jones matrix. The Jones vector of linearly polarized light passing through the polarizer can be described as $J_0 = E_0[1,0]^T$, where E_0 is the electric field amplitude of the incident beam. The Jones matrix of the EOM can be expressed as follows:[36]

$$J_{EOM} = \begin{bmatrix} \cos(\delta(t)/2) & -i\sin(\delta(t)/2) \\ -i\sin(\delta(t)/2) & \cos(\delta(t)/2) \end{bmatrix} \quad (2)$$

In the EOM, the phase retardation between the transmission axis and the vertical direction can be expressed as: $\delta(t) = \delta_0 \sin \omega_m t$, where ω_m is the modulation frequency. The EOM time-varying birefringence amplitude δ_0 can be described as $\delta_0 = 2\pi\nu_p n^3 \gamma V(t)/c$, where ν_p is the frequency of the probe laser, n is the refractive index of the electro-optic material, γ is the electro-optic coefficient, and $V(t)$ is the sinusoidal modulation function applied to the EOM.[37] Assuming that the incident light intensity is $I_0 = {E_0}^2$, according to Marius' law and the principle of polarized light propagation,[38] the intensity of the light received by the photodetector is given as follows:

$$I = I_0 \sin^2(\theta + \delta(t)/2) \quad (3)$$

Because the optical rotation angle and modulation amplitude were small, an approximation was applied.[39] The ideal output light intensity of the system can be obtained as follows:

$$I \approx \frac{1}{8} I_0 {\delta_0}^2 + \theta I_0 \delta_0 \sin \omega_m t - \frac{1}{8} {\delta_0}^2 \cos(2\omega_m t) \quad (4)$$

Evidently, the optical rotation angle θ can be determined by measuring the first harmonic signal of the detection system output signal.

The design and operational principles of the TFLN-based EOM are illustrated in Fig. 1(b). We utilized a periodic nanopillar array with specifically optimized parameters on the TFLN waveguide to achieve sub-wavelength resonators that modulate the incident light propagating through the thin film. The dashed box denotes the unit cell of the nanopillar, where P represents the unit period, D is the diameter of the nanopillar, and H is the nanopillar thickness. The metasurface is a centrally symmetric structure that minimizes the sensitivity to fabrication errors owing to complex structures.[40] The incident light diffracts into the TFLN waveguide through the nanopillar array structure, and a strong coupling resonance occurs when the wave vectors of the structure match the mode in the waveguide. A high-frequency voltage is applied *via* metal electrodes, which alters the refractive index of the material through the linear electro-optic effect, also known as the Pockels effect. To optimize the resonance at 795 nm, we iteratively sweep the design parameters one at a time. As the thickness of the LN waveguide layer was fixed, three optimizable design parameters were required: the nanopillar diameter, nanopillar height, and unit cell period. Initially, the unit cell period and nanopillar height were set to 440 nm and 120 nm, respectively, to ensure excitation at a wavelength of 795 nm. Subsequently, the unit cell period and height were swept to identify narrow and deep absorption dips in the transmission spectrum. The simulated transmission is presented as a function of wavelength and nanopillar parameters and the other two parameters remained fixed as shown in Fig. 2(a–c), respectively. With the change in the nanopillar diameter and height, the narrow resonance in the wavelength range shifted only slightly within 10 nm, whereas the variation in the unit cell period resulted in a large shift in the resonant wavelength. Furthermore, increasing the thickness of the TFLN helped to restrict more of the optical field, potentially leading to a narrower resonance width. The optimized design parameters are indicated by the black circles: D = 270 nm, H = 120 nm, and P = 438 nm. In Fig. 2(d) and (e), we present the transmission and phase (ϕ) spectra. Fig. 2(d) shows the transmission spectra and associated field distributions for the two absorption peaks. Evidently, the electric field is mainly localized within the nanopillar structures at the resonant wavelength of 763 nm. The black dashed box highlights the electric and magnetic field distributions at the resonant wavelength of 795 nm, where the electric field is primarily confined to the waveguide. Fig. 2(e) shows the phase spectra of the transmitted light caused by the refractive index under a ±200 V voltage, and the theoretical phase modulation span of ±1.3 rad is obtained at the resonant wavelength. To further study the principle of the structure, the relationship between the incident angle and transmission spectrum is shown in ESI Fig. S2 and S3.† To simulate the taper angle in the processing of LN materials, the structure was configured as a circular truncated cone with a 67° taper angle instead of a cylindrical shape with a 90° angle during optimization. This configuration accurately reflects the characteristics of the samples produced in actual manufacturing processes.

3. Experiment and results

The designed EOM was manufactured using a commercial x-cut TFLN wafer (NANOLN). A 600 nm-thick $LiNbO_3$ layer was directly bonded to a 2 μm layer of SiO_2, with a 500 μm-thick

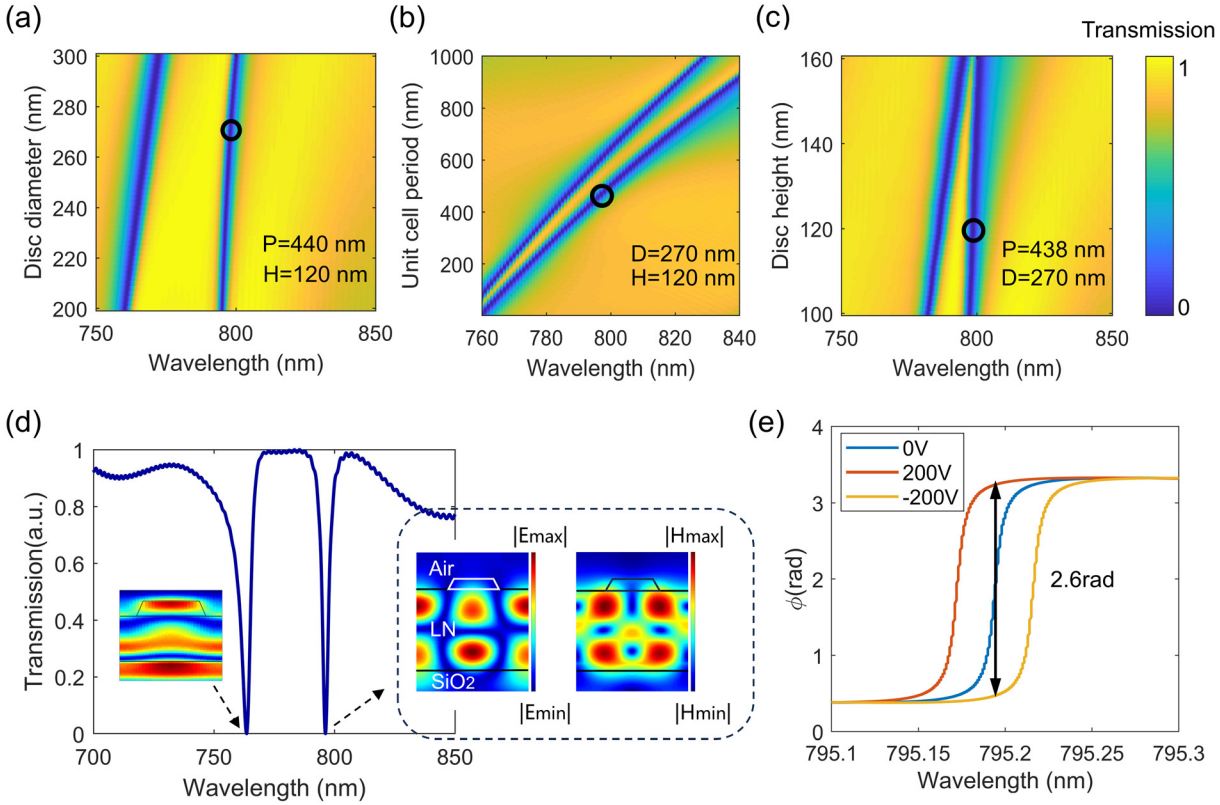

Fig. 2 Design and optimization of the GMR metasurface. (a–c) Color maps of the calculated transmission amplitude as a function of the wavelength and (a) nanopillar diameter, *D*, (b) unit cell period, *P*, and (c) nanopillar height, *H*. Black circles represent the selected parameters: *D* = 270 nm, *P* = 438 nm, and *H* = 120 nm. (d) Transmission spectrum and cross-sectional view of the field distribution at different resonant wavelengths. (e) Simulated transmission phase spectra of the GMR metasurface corresponding to a driving voltage of ±200 V.

single-crystal quartz substrate. An electron beam lithography (EBL) resist was deposited on the 600 nm-thick LN film. Following EBL exposure and development, Cr was deposited to serve as a hard-mask etch-stop layer. The lift-off process was then employed to remove Cr and resist the non-structural regions. Subsequent reactive ion etching processes were used to achieve a 120 nm deep etch into $LiNbO_3$. The electrodes were etched using ultraviolet (UV) photolithography, and an evaporation-coated 20 nm thick Cr layer served as an adhesive. Finally, electrodes consisting of a 50 nm thick Au layer were deposited on the surface by electron-beam evaporation and completed using a lift-off process. ESI Fig. S1(a) and S1(b)† display magnified images captured using a COMS camera and scanning electron microscopy (SEM) images of the fabricated metasurface, respectively.

Measurements were conducted on the fabricated metasurface prior to the electric field poling of the devices. Due to the anisotropic properties of LN materials,[41] the polarization angle of the incident linearly polarized light may lead to a shift in the absorption peaks, thereby affecting the modulation efficiency. In Fig. 3(a), we present the variations in the transmission spectra of the structure at different polarization angles. To further observe the influence of the polarization angle on the resonant wavelength, the simulated and measured transmission spectra at different polarization angles varied in 10° increments are shown in Fig. 3(b) and (c), respectively. These results demonstrate the consistency and uniformity between the test spectra and the simulation. A polarization angle of 0° indicates that the incident light is polarized along the extraordinary axis (n_e), while 90° corresponds to polarization along the ordinary axis (n_o). As the polarization angle changes from 0° to 90°, the corresponding refractive index gradually increases ($n_o > n_e$),[41] causing a redshift in the resonance. Experimentally, the red shifts of the two absorption peaks are 19 nm and 12 nm, respectively. Additionally, the variation in the resonance peaks as the polarization angle changes from 0° to 40° is negligible, which can be attributed to the centrosymmetric design of the structure, minimizing its sensitivity to polarization. From the measurement results, the maximum resonance depth of about 60% is achieved at the resonant wavelength of 795.8 nm. A high resonance depth (the difference between the peak and trough of the resonance spectrum) can be used to enhance modulation. Furthermore, we experimentally determined the corresponding quality factors for 0° (Q = 172 and Q = 161 for 776.7 nm and 805.2 nm, respectively) and 90° (Q = 166 and Q = 204 for 795.8 nm and 816.7 nm), see Fig. 3(d). In the experiment, the laser beam emitted by a supercontinuum light source (SM-250-

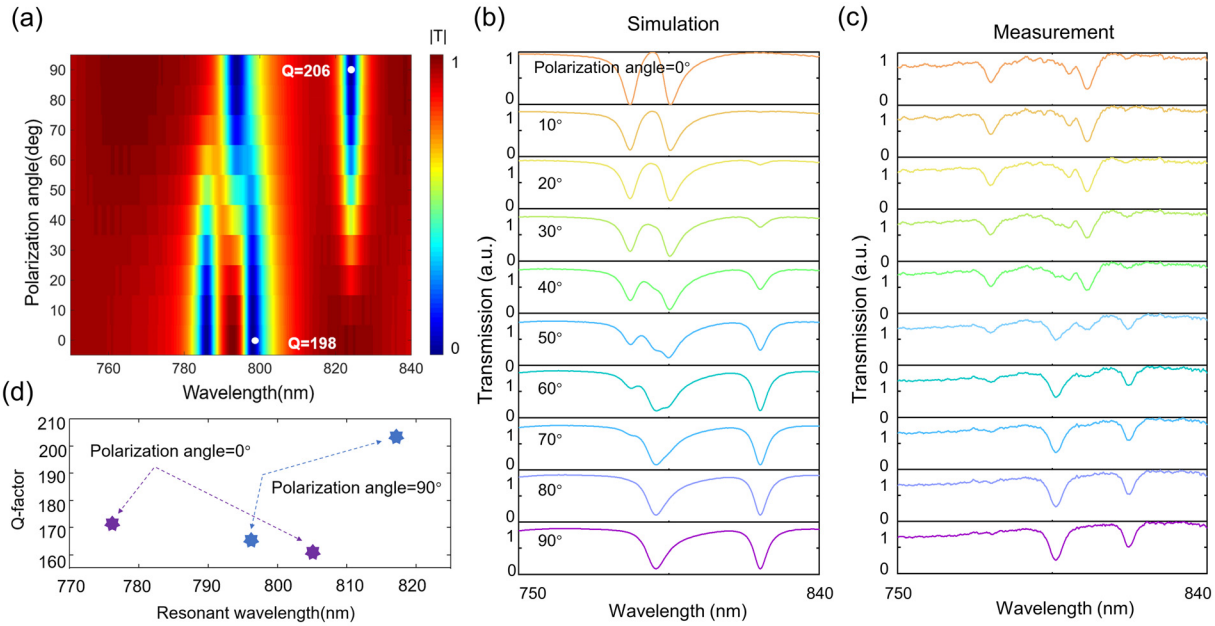

Fig. 3 Characterization of the metasurface. (a) Calculated transmission as a function of the polarization angle and wavelength. (b) Simulated and (c) measured transmission spectra at different polarization angles. (d) Experimentally extracted quality factors for different resonant wavelengths at vertical polarization.

VIS-IR) was first linearly polarized using a high extinction ratio polarizer, and then it was passed through the fabricated device. The transmitted light was subsequently detected and analyzed using a spectrometer (Ocean Optics, USB4000). The slight discrepancies between the experimental and simulated spectra could be attributed to structural manufacturing errors.

In the following, we present the tuning properties of the LN free-space modulator when a sinusoidal AC voltage is applied to the electrodes to achieve maximum modulation. In the experiments, the samples were mounted on a sample holder connected to a six-degree-of-freedom stage. A Distributed Bragg Reflector (PH795DBR) laser with a center wavelength of approximately 795 nm was used to generate the free-space laser beam. The collimator light from the laser was focused using a 10× microscope objective to form a spot slightly smaller than the metasurface modulator area. The needles were positioned to apply a voltage to the electrodes *via* a three-axis stage. The connection to the modulating power supply was established using a signal generator (KEYSIGHT 33500B) and a voltage amplifier (Thorlabs HVA200) *via* a crocodile clip wire. Linearly polarized light passing through the sample was received using a photodetector (Thorlabs PDA100A2), which was connected to a lock-in amplifier (MFLI 500 kHz/5 MHz) through a high extinction ratio Glan-Taylor prism. The azimuth of the principal polarizer axis was precisely adjusted to 45° relative to the fast-axis of the sample to maximize the phase delay. The phase modulation introduced by the Pockels effect is converted into polarization changes, which can be measured by detecting the intensity variation of light after it passes through an analyzer with the help of a photodetector.[30] Based on the maximum and minimum values of the received signal from the photodetector, the phase modulation amplitude is calculated to be approximately 0.063 rad under a ±200 V voltage with a 100 kHz modulation frequency, which is sufficient to achieve the modulation of an extremely small optical rotation angle.[44] The details and photographs of the experimental setup are shown in ESI Fig. S4.† The experimental results for the modulation performance of the sample are shown in Fig. 4(a–d). The frequency spectrum and the time-domain signals extracted by the photodiode were tested at frequencies of 5 kHz, 100 kHz, 300 kHz, and 500 kHz. Distinct peaks in the frequency spectrum at the corresponding frequencies are observed, and the time-domain signal is clearly defined. At a modulation frequency of 5 kHz, the modulation amplitude variation reached 18 mV. Additionally, a second harmonic signal at 200 kHz (twice the fundamental frequency of 100 kHz) is observed, which is attributed to the system's nonlinear response (Fig. 4(b)). The amplitude of the higher-order harmonic signals can be controlled by adjusting the driving voltage. With increasing modulation frequency, the modulation response and time-domain signal quality gradually degrade. Nevertheless, the modulation performance of the device at a frequency of 300 kHz was sufficient to satisfy the frequency requirements for modulating optical rotation signals in atomic sensors. ESI Fig. S5† presents the modulation performance results for the other samples.

The sensitivity of the optical rotation angle signal was measured using the fabricated device. To evaluate the suppression effect of the modulator on low-frequency noise, we compared the sensitivity of the detection system under the same experimental conditions, with and without modulation. A schematic of the experimental setup based on the compact

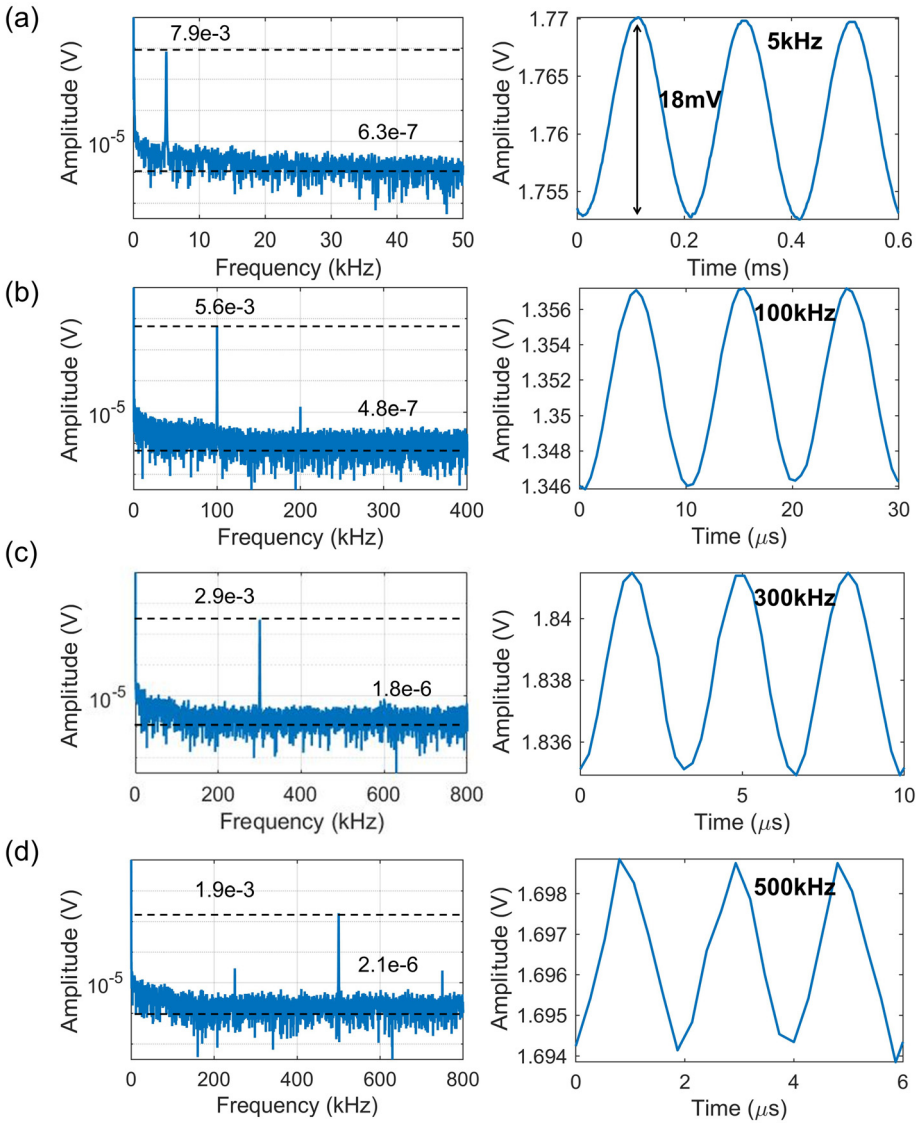

Fig. 4 Frequency spectrum response and time-domain waveform. (a) Frequency spectrum response and time-domain waveform at a 5 kHz sinusoidal modulation signal, with the modulation amplitude exhibiting a variation of 18 mV. (b) Frequency spectrum response and time-domain waveform at 100 kHz. (c) Frequency spectrum response and time-domain waveform at 300 kHz. (d) Frequency spectrum response and time-domain waveform at 500 kHz.

modulator is shown in Fig. 5(a). In the experiment, a probe beam generated with a DBR laser propagated through a polarization-maintaining fiber with a 300 μm spot collimator to match the sample size. A magneto-optical crystal with a Verdet constant of 60 rad T^{-1} m^{-1} at 795 nm was utilized to generate a constant and easy-to-control optical rotation angle to replace the alkali metal atomic cell for sensitivity testing of a small optical angle.[8] The Faraday effect demonstrates the ability of a magneto-optical material to induce rotation in the polarization plane of linearly polarized light when exposed to a magnetic field parallel to the direction of incident beam propagation. The rotation angle θ is given by $\theta = VBL$, where B is the magnetic field strength and L is the axial length of the magneto-optical material.[42] Specifically, we positioned a 20 mm long magneto-optic crystal within a small cylindrical magnetic shield barrel to attenuate the ambient magnetic field. The external magnetic field applied to the magneto-optical crystal was generated by a 120-turn solenoid coil driven by a signal generator (KEYSIGHT 33500B) supplying a 10 Hz sinusoidal signal to generate a calibrated optical rotation angle signal of 4.1×10^{-4} rad. The probe beam with the optical rotation angle θ was detected using a photodiode amplifier detector (Thorlabs PDA100A2). According to the EOM detection principle, the first harmonic component is proportional to θ. This component was extracted and demodulated by a lock-in amplifier (Zurich Instruments MFLI). To further validate the effectiveness of the modulation detection method and the feasibility of the fabricated device for improving the sensitivity, we

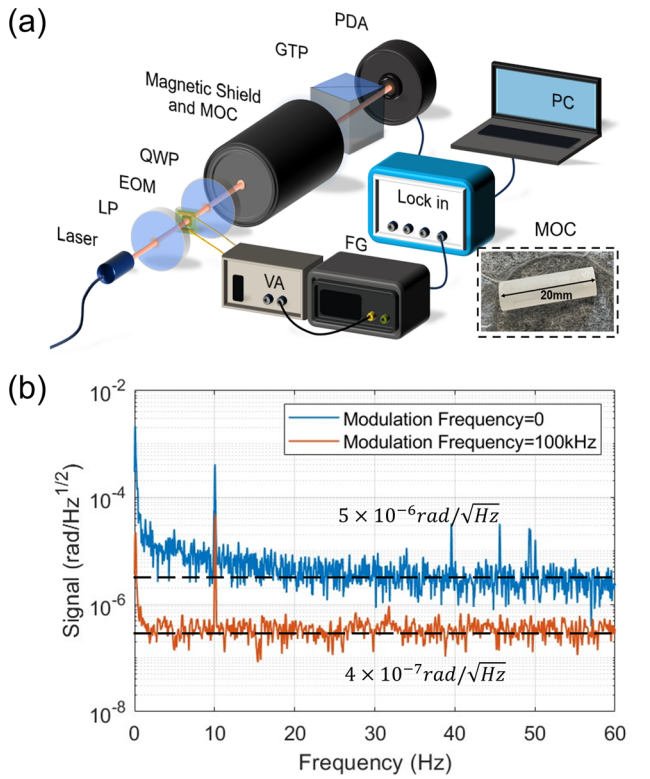

Fig. 5 (a) Schematic representation of the experimental setup. LP: linear polarizer; QWP: quarter-wave plate; MOC: magneto-optical crystal; GTP: Glan Taylor prism; PDA: photodiode amplifier; VA: voltage amplifier; FG: function generator; Lock in: lock-in amplifier; and PC: personal computer for data acquisition. (b) Optical rotation angle measurement sensitivities with 100 kHz modulation using the fabricated ultracompact modulator with and without modulation.

measured the sensitivity with modulation at a 100 kHz frequency and without modulation. The experimental results are shown in Fig. 5(b). It is evident that the system exhibited significant noise when using the balanced polarimetry method without modulation, which employs the same magneto-optical crystal and achieves a sensitivity of approximately 5×10^{-6} rad $Hz^{-1/2}$. The EOM detection method achieved a theoretical sensitivity of $\sim 4 \times 10^{-7}$ rad $Hz^{-1/2}$ using the compact device with a modulation frequency of 100 kHz. This result indicates that the compact EOM effectively reduces low-frequency noise in the detection system and achieves an ultrahigh sensitivity.

The modulation efficiency is significantly influenced by the drive voltage and the distance between the electrodes, necessitating a higher voltage owing to the large gap between the electrodes in this study. Furthermore, fabrication errors during the nanofabrication process may affect the size and vertical alignment of the nanopillars. Because the resonant structure is highly sensitive to the periodic dimensions, the resonant wavelength deviation can adversely impact the modulation quality and reduce the SNR. To further improve the SNR, it is essential to optimize the manufacturing process to minimize fabrication errors. Additionally, the electro-optic coefficient of LN material limits the refractive index variation, which is expressed as $|\Delta n| = n_m^3 \gamma V/2d$, where γ is the electro-optic coefficient of the material,[29] n_m is the refractive index of electro-optic materials in the absence of applied voltage, V is the voltage applied in the tuning field across the distance d of the electrodes. In the future, the use of materials with higher electro-optic coefficients[27,45] and optimized electrode arrangements may enable greater tunability and lower driving voltage, which facilitate integration. Nevertheless, the proposed approach offers a significant reduction in volume, shrinking the size of EOMs from over 20 cm^3 to less than 0.5 cm^3 when compared to traditional bulky modulators.

4. Conclusion

The objectives of this study were to improve the low-frequency detection sensitivity of atomic sensors and overcome the challenges posed by the bulky size and poor integration of conventional modulators. We proposed a TFLN EOM based on a GMR composed of a subwavelength structure array to realize high-frequency signal modulation. A nanopillar array was fabricated on a 600 nm x-cut thin LN film. The device achieved efficient phase tuning, with a phase modulation amplitude of 0.063 rad under a ±200 VAC driving voltage at a 100 kHz modulation frequency. Simultaneously, the optical rotation angle measurement achieved a sensitivity of 4×10^{-7} rad $Hz^{-1/2}$ at a modulation frequency of 100 kHz using the compact EOM, outperforming the non-modulated method under the same working conditions. Compared with passive integrated metasurface devices, this study introduces a novel approach to achieve low-frequency noise suppression by designing an active device for the modulation of free-space beams in a compact manner. A large area metasurface was designed to match the larger beam spot sizes, which is beneficial for practical applications. Moreover, this method can be applied to the all-optical modulation of spin polarization to generate light-shift modulation.[43] Specifically, the modulator is fabricated using pure dielectric materials, ensuring its compatibility with on-chip insulating silicon technology and integration with nanophotonic devices. This approach addresses the challenge of integrating bulky modulators into optical systems and provides a new pathway for achieving ultra-high sensitivity in miniaturized atomic sensors through compact packaging of the modulator.

Author contributions

All authors have accepted responsibility for the entire content of this manuscript and approved its submission.

Informed consent

Informed consent was obtained from all individuals included in this study.

Ethical approval

The conducted research is not related to either human or animal use.

Data availability

The data supporting this article have been included as part of the ESI.†

Conflicts of interest

The authors state no conflicts of interest.

Acknowledgements

This research was supported by the General Program of the National Natural Science Foundation of China (62373028), the Beijing Natural Science Foundation (4232071), the Zhejiang Provincial Natural Science Foundation of China (LZ24F050007).

References

1 G. Bison, N. Castagna, A. Hofer, P. Knowles, J. L. Schenker, M. Kasprzak, H. Saudanm and A. Weis, *Appl. Phys. Lett.*, 2009, **95**, 17.
2 Z. Di, X. Chen, S. Pu, X. Hu and Y. Xia, *Appl. Phys. Lett.*, 2006, **89**, 21.
3 O. Alem, T. H. Sander, R. Mhaskar, J. LeBlanc, H. Eswaran, U. Steinhoff, Y. Okada, J. Kitching, L. Trahms and S. Knappe, *Phys. Med. Biol.*, 2015, **60**, 4797.
4 T. W. Kornack, R. K. Ghosh and M. V. Romalis, *Phys. Rev. Lett.*, 2005, **95**, 230801.
5 T. E. Chupp, P. Fierlinger, M. J. Ramsey-Musolf and J. T. Singh, *Rev. Mod. Phys.*, 2019, **91**, 015001.
6 P. D. Schwindt, B. Lindseth, S. Knappe, V. Shah, J. Kitching and L. A. Liew, *Appl. Phys. Lett.*, 2007, **90**, 8.
7 Y. Sebbag, E. Talker, A. Naiman, Y. Barash and U. Levy, *Light: Sci. Appl.*, 2021, **10**, 54.
8 Y. Xu, Y. Xu, J. Sun, Y. Mao, Z. Chai and J. Li, *Adv. Opt. Mater.*, 2024, **12**, 2301353.
9 J. Hu, Z. Liang, P. Zhou, L. Liu, G. Hu, P. Du and M. Ye, *Opt. Lett.*, 2024, **49**, 3364.
10 Z. Liang, J. Hu, P. Zhou, L. Liu, G. Hu, A. Wang and M. Ye, *Microsyst. Nanoeng.*, 2024, **10**, 101.
11 J. M. Brown, S. J. Smullin, T. W. Kornack and M. V. Romalis, *Phys. Rev. Lett.*, 2010, **105**, 151604.
12 G. Vasilakis, J. M. Brown, T. W. Kornack and M. V. Romalis, *Phys. Rev. Lett.*, 2009, **103**(26), 261801.
13 L. Duan, J. Fang, R. Li, L. Jiang, M. Ding and W. Wang, *Opt. Express*, 2015, **23**, 32481.
14 L. Xing, Y. Zhai, Y. Fu, T. Song, F. Liu, Q. Cai and W. Quan, *Meas. Sci. Technol.*, 2020, **32**(2), 025112.
15 D. Chen, Y. Yang, W. Jin, X. Wang, Y. Liu and T. Wang, *Opt. Express*, 2021, **29**, 44093.
16 Z. Cui, Y. Wang, Y. Liu, M. Jin, J. Sun, Y. Zhai, X. Zhou and Z. Chai, *Nanophotonics*, 2024, **13**(23), 4255–4265.
17 Y. Huang, T. Xiao, S. Chen, Z. Xie, J. Zheng, J. Zhu, Y. Su, W. Chen, K. Liu, M. Tang, P. Müller-Buschbaum and L. Ling, *Opto-Electron. Adv.*, 2023, **6**(7), 220073.
18 M. Zhang, M. Pu, F. Zhang, Y. Guo, Q. He, X. Ma, Y. Huang, X. Li, H. Yu and X. Luo, *Adv. Sci.*, 2018, **5**(10), 1800835.
19 S. Jiao, J. Liu, L. Zhang, F. Yu, G. Zuo, J. Zhang, F. Zhao, W. Lin and L. Shao, *Opto-Electron. Sci.*, 2022, **1**(9), 220010.
20 C. Damgaard-Carstensen, M. Thomaschewski and S. I. Bozhevolnyi, *Nanoscale*, 2022, **14**, 11407–11414.
21 D. Renaud, D. R. Assumpcao, G. Joe, A. Shams-Ansari, D. Zhu, Y. Hu, N. Sinclair and M. Loncar, *Nat. Commun.*, 2023, **14**, 1496.
22 H. Weigand, V. V. Vogler-Neuling, M. Reig Escalé, D. Pohl, F. Richter, A. Karvounis, F. Timpu and R. Grange, *ACS Photonics*, 2021, **8**, 3004.
23 J. Liu, L. Qu, W. Wu, C. Jin, Z. Chen, Z. Gu, W. Liu, C. Wang, D. Zheng, H. Liu, W. Cai, M. Ren and J. Xu, *Nanophotonics*, 2024, **13**, 1503.
24 K. Koshelev, S. Lepeshov, M. Liu, A. Bogdanov and Y. Kivshar, *Phys. Rev. Lett.*, 2018, **121**, 193903.
25 M. S. Bin-Alam, O. Reshef, Y. Mamchur, M. Z. Alam, G. Carlow, J. Upham, B. T. Sullivan, J.-M. Ménard, M. J. Huttunen, R. W. Boyd and K. Dolgaleva, *Nat. Commun.*, 2021, **12**, 974.
26 K. Koshelev and Y. Kivshar, *ACS Photonics*, 2020, **8**, 102.
27 I. C. Benea-Chelmus, S. Mason, M. L. Meretska, D. L. Elder, D. Kazakov, A. Shams-Ansari, L. R. Dalton and F. Capasso, *Nat. Commun.*, 2022, **13**, 3170.
28 I. K. Kominis, T. W. Kornack, J. C. Allred and M. V. Romalis, *Nature*, 2003, **422**, 596.
29 H. Xia, Z. Li and C. Chen, *Opt. Commun.*, 2024, **554**, 130178.
30 T. A. Maldonado, *Handb. Opt.*, 1995, **2**, 13.
31 L. Huang, R. Jin, C. Zhou, G. Li, L. Xu, A. Overvig, F. Deng, X. Chen, W. Lu, A. Alù and A. E. Miroshnichenko, *Nat. Commun.*, 2023, **14**, 3433.
32 J. Hu, Z. Liang, P. Zhou, L. Liu, G. Hu and M. Ye, *Nanophotonics*, 2024, **13**(23), 4231–4242.
33 M. P. Ledbetter, I. M. Savukov, V. M. Acosta, D. Budker and M. V. Romalis, *Phys. Rev. A:At., Mol., Opt. Phys.*, 2008, **77**, 033408.
34 I. M. Savukov, S. J. Seltzer, M. V. Romalis and K. L. Sauer, *Phys. Rev. Lett.*, 2005, **95**, 063004.
35 K. Kamada, Y. Ito, S. Ichihara, N. Mizutani and T. Kobayashi, *Opt. Express*, 2015, **23**, 6976.
36 M. Tian, W. Quan, L. Jiang, J. Liu, Y. Chai, Z. Lu and X. Zhao, *Opt. Lett.*, 2023, **48**, 3075.
37 H. Qi, A. Wei and D. Yuan, *Mater. Sci. Eng., B*, 2005, **122**, 246.
38 M. Born and E. Wolf, *Principles of Optics: Electromagnetic Theory of Propagation, Interference and Diffraction of Light*, Elsevier, 2013.

39 H. Yao, Y. Li, D. Ma, J. Cai, J. Zhao and M. Ding, *Opt. Express*, 2018, **26**, 28682.
40 Y. Ju, W. Zhang, Y. Zhao, X. Deng and H. Zuo, *Opt. Mater.*, 2024, **148**, 114928.
41 J. Yi, C. Guo, Z. Ruan, G. Chen, H. Wei, L. Lu, S. Gong, X. Pan, X. Shen, X. Guan, D. Dai, K. Zhong and L. Liu, *Light: Sci. Appl.*, 2024, **13**, 147.
42 X. Yang, X. Xin, Y. Hao, Z. Zhang, Q. Hu, X. Fu and X. Tao, *CrystEngComm*, 2024, **26**, 3311.
43 X. Li, B. Han, K. Zhang, Z. Liu, S. Wang, Y. Yan and J. Lu, *Phys. Rev. Appl.*, 2024, **21**, 014023.
44 Y. Hu, X. Liu, Y. Li, H. Yao, L. Dai, B. Yang and M. Ding, *J. Phys. D:Appl. Phys.*, 2017, **50**, 265001.
45 N. Sun, D. G. Sun, D. Wu, Y. Guo, Y. Fan, F. Zou, M. Pu and X. Luo, *Laser Photonics Rev.*, 2024, **18**(3), 2300937.
46 H. Yao, Y. Li, D. Ma, J. Cai, J. Zhao and M. Ding, *Opt. Express*, 2018, **26**(22), 28682–28692.